

Horizon physics of quasi-one-dimensional tilted Weyl cones on a lattice

Viktor Könye¹, Corentin Morice^{2,3}, Dmitry Chernyavsky¹, Ali G. Moghaddam^{4,5},
 Jeroen van den Brink^{1,6} and Jasper van Wezel²

¹*Institute for Theoretical Solid State Physics, IFW Dresden and Würzburg-Dresden Cluster of Excellence ct.qmat, Helmholtzstrasse 20, 01069 Dresden, Germany*

²*Institute for Theoretical Physics and Delta Institute for Theoretical Physics, University of Amsterdam, 1090 GL Amsterdam, The Netherlands*

³*Laboratoire de Physique des Solides, CNRS UMR 8502, Université Paris-Saclay, F-91405 Orsay Cedex, France*

⁴*Department of Physics, Institute for Advanced Studies in Basic Sciences (IASBS), Zanjan 45137-66731, Iran*

⁵*Computational Physics Laboratory, Physics Unit, Faculty of Engineering and Natural Sciences, Tampere University, FI-33014 Tampere, Finland*

⁶*Institute for Theoretical Physics, TU Dresden, 01069 Dresden, Germany*



(Received 8 June 2022; accepted 23 August 2022; published 26 September 2022)

To simulate the dynamics of massless Dirac fermions in curved space-times with one, two, and three spatial dimensions, we construct tight-binding Hamiltonians with spatially varying hoppings. These models represent tilted Weyl semimetals where the tilting varies with position, in a manner similar to the light cones near the horizon of a black hole. We illustrate the gravitational analogies in these models by numerically evaluating the propagation of wave packets on the lattice and then comparing them to the geodesics of the corresponding curved space-time. We also show that the motion of electrons in these spatially varying systems can be understood through the conservation of energy and the quasiconservation of quasimomentum. This picture is confirmed by calculations of the scattering matrix, which indicate an exponential suppression of any noncontinuous change in the quasimomentum. Finally, we show that horizons in the lattice models can be constructed also at finite energies using specially designed tilting profiles.

DOI: [10.1103/PhysRevResearch.4.033237](https://doi.org/10.1103/PhysRevResearch.4.033237)

I. INTRODUCTION

Analogies in physics, between seemingly unrelated systems, can not only lead to advances in the understanding of these systems, but also contribute to the development of new applications. Among the known analogies, a particularly fruitful connection has been made between gravitational physics and condensed-matter systems. Such an analogy was first proposed to study the extraordinary consequences of the curvature of space-time on quantum fields, namely, the Hawking and Unruh radiations, which are in practice too weak to be measured [1–5]. This has attracted considerable interest in recent years from various directions, and gravitational analogies have been considered in many contexts, including electronic, acoustic, optical, and even magnetic and superconducting settings [6–29]. Particularly, implementations using Bose-Einstein condensates have been used to mimic Hawking and Unruh radiations [30–32].

Recent attempts have been made to exploit developments in the prediction and synthesis of Weyl semimetals (WSMs), whose low-energy electronic states can be described by the

Weyl equation [33]. In particular, it has been shown that a position-dependent tilting of the Weyl cone in a way to create neighboring regions with type-I and type-II WSM can lead to a black hole analog [34–39]. This analogy can be understood by thinking of the Weyl cones in the material as the light cones of a curved space-time, thus the boundary of the WSMs of different types as the horizon. Exactly at the transition point between type I and type II, the Weyl cones are tangent to the zero-energy surface, a situation called type-III WSM. One study has shown that the band structure of $\text{Zn}_2\text{In}_2\text{S}_5$ has such a property that makes it promising for the realization of a black hole horizon [38]. Proposals for tilting the cone as a function of real space include the use of structural distortions, spin textures, and external position-dependent driving [36,40–44]. Most works until recently assumed that, given that the tilting changes smoothly, one can define band dispersions varying as a function of space. Since WSMs are defined on a lattice, and the tilting variation implies the lack of translational symmetry, and therefore of a reciprocal space, this kind of assumption is imprecise. This was addressed subsequently by studying a class of tight-binding models with position-dependent nearest-neighbor hopping concentrating on the single-band one-dimensional (1D) cases [45–47].

Here we go beyond previous works by introducing two-band tilted Weyl cones defined on lattices, in one, two, and three spatial dimensions, and investigate their properties. Taking into account the lattice explicitly is motivated by physical Weyl semimetals having band structures that are ultimately

Published by the American Physical Society under the terms of the [Creative Commons Attribution 4.0 International](https://creativecommons.org/licenses/by/4.0/) license. Further distribution of this work must maintain attribution to the author(s) and the published article's title, journal citation, and DOI.

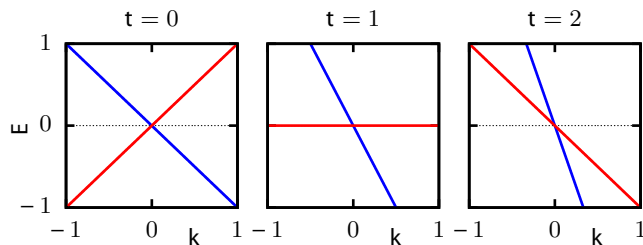


FIG. 1. Energy dispersion of a tilted Weyl Hamiltonian in 1D as in Eq. (2) for three different tilting parameters t .

defined on discrete lattices, which play an important role near horizons when wave packets start slowing down exponentially [45]. Moreover, lattice formulations allow for numerically tracking wave-packet dynamics with the very efficient Chebyshev expansion method [48,49]. We discuss the consequences of different ways of creating Weyl cones on a lattice, as such models are not unique. We connect the low-momentum limit of these models to gravitational physics and show they are equivalent to Dirac equations in a curved space-time background. We emphasize that, due to the two-band nature of our models, the connection to the relativistic Dirac equation is more explicit than previously studied incarnations. Then we explore the propagation of wave packets in these models and compare them to geodesics of gravitational systems. Finally, we calculate the scattering matrix in the 1D models and discuss the large quantitative and qualitative differences arising between the different types of models.

II. TILTED WEYL CONE MODELS

In order to simulate horizons in lattice models, we construct inhomogeneous tight-binding models hosting tilted Weyl cones, whose tilting depends on the position in real space. The horizon appears at the points where the tilted cone goes through the Fermi level, i.e., where the WSM goes from type I to type II. We want the local low-energy effective Hamiltonian to correspond to the following tilted Weyl continuum Hamiltonian:

$$H = \boldsymbol{\sigma} \cdot \mathbf{k} - \sigma_0(\mathbf{t} \cdot \mathbf{k}), \quad (1)$$

where \mathbf{k} is the quasimomentum, σ_i are the Pauli matrices acting on a pseudospin representing different orbitals, and \mathbf{t} is the tilting vector. The energy dispersion of this Hamiltonian is

$$E_{\pm} = \pm|\mathbf{k}| - \mathbf{t} \cdot \mathbf{k}. \quad (2)$$

For $\mathbf{t} = \mathbf{0}$ we get an untilted Weyl cone. In the one-dimensional case (see Fig. 1), for $t > 0$ the spectrum is tilted clockwise, and at $t = 1$, one of the branches of the cone becomes completely flat and the group velocity in this branch becomes zero.

In this section, first we discuss how to construct simple lattice models in one (1D), two (2D), and three dimensions (3D) that host one or several tilted Weyl cones. We then show how these Hamiltonians are connected to the Dirac equation in a curved space-time when the tilting changes as a function

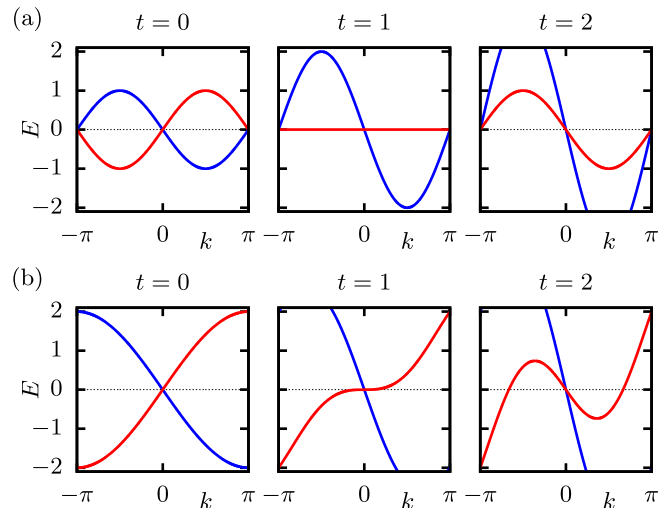


FIG. 2. Energy dispersion of (a) H_1^{1D} as in Eq. (5a) and (b) H_2^{1D} as in Eq. (5b) for three different tilting parameters t . The three tiltings correspond to the untilted type-I node, the node at the horizon, and the overtilted type-II node.

of position. With this we get lattice models that describe the motion of electrons in a curved background.

A. 1D lattice models

We start with presenting 1D models that have tilted Weyl cones at low energies. In principle, there are many ways to put the Eq. (1) Hamiltonian on a lattice with the same low-energy effective Hamiltonian around $k = 0$ but with different behavior at $|k| \gg 0$. Here, we study the following two models:

$$\mathcal{H}_1^{1D} = \sum_x \frac{i}{2} c_{x+1}^\dagger (\sigma_x - t\sigma_0) c_x + \text{H.c.}, \quad (3a)$$

$$\mathcal{H}_2^{1D} = \sum_x c_x^\dagger \frac{\sigma_z}{2} c_x + c_{x+1}^\dagger \left[-\frac{\sigma_z}{2} + \frac{i}{2} (\sigma_x - t\sigma_0) \right] c_x + \text{H.c.}, \quad (3b)$$

where $c_x = (c_{x\uparrow}, c_{x\downarrow})$ is the annihilation operator of an electron at site $x \in \mathbb{Z}$ with pseudospin \uparrow or \downarrow .

For a constant position-independent tilt, the Bloch Hamiltonians of these after Fourier transformation are given as

$$H_1^{1D} = (\sigma_x - t\sigma_0) \sin k, \quad (4a)$$

$$H_2^{1D} = (\sigma_x - t\sigma_0) \sin k + \sigma_z(1 - \cos k), \quad (4b)$$

which give the following dispersion relations (see Fig. 2):

$$E_{1\pm}^{1D} = \pm|\sin k| - t \sin k, \quad (5a)$$

$$E_{2\pm}^{1D} = \pm\sqrt{\sin^2 k + (1 - \cos k)^2} - t \sin k. \quad (5b)$$

Both these models converge to Eq. (1) for $k \rightarrow 0$ and describe the same kind of tilted Weyl cone, but they differ away from $k = 0$. In particular, H_1^{1D} has a second Weyl cone at the edge of the Brillouin zone, unlike H_2^{1D} which only has one cone. In both cases if the tilting parameter is less (more) than 1 we get type-I (type-II) Weyl nodes. In the overtilted

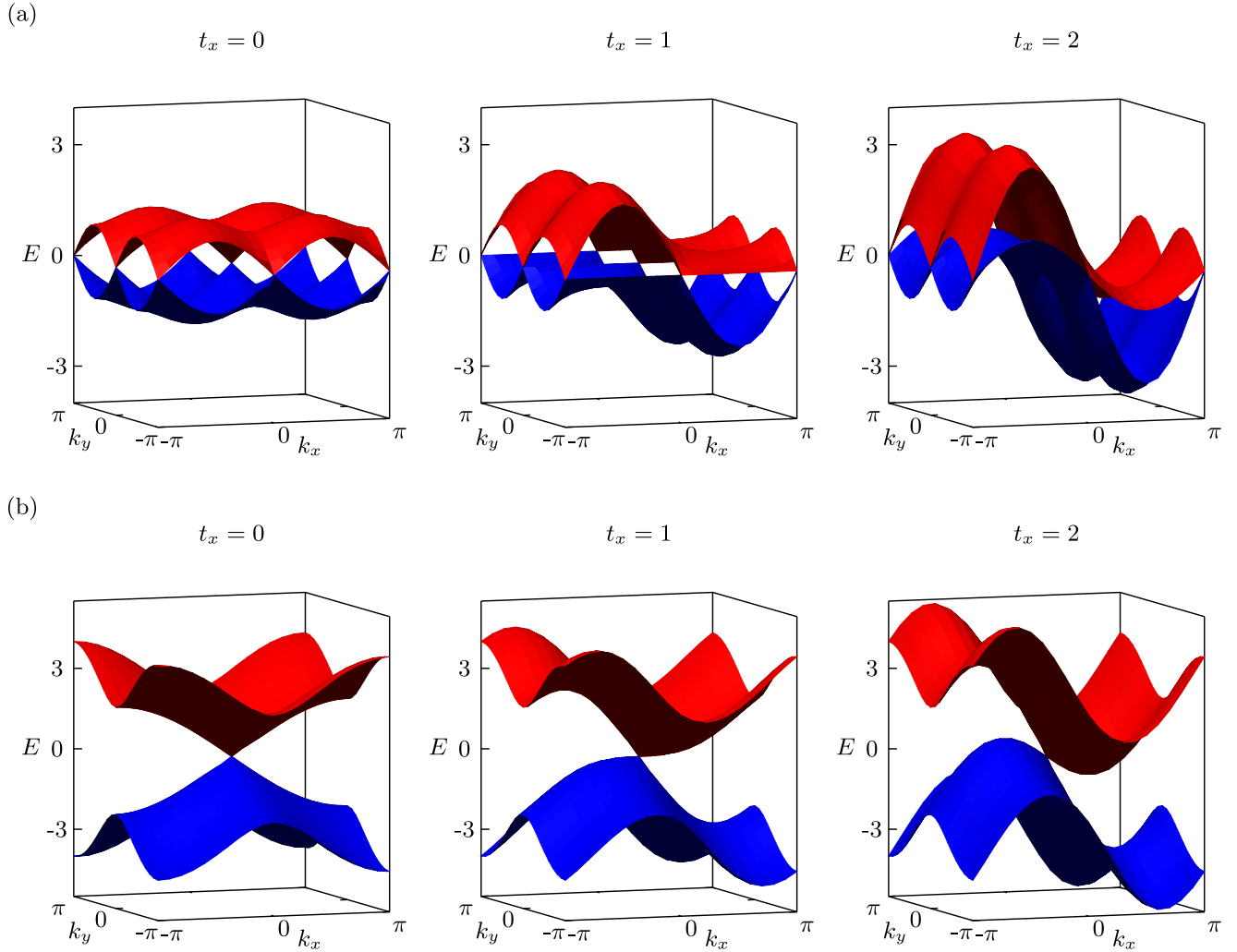


FIG. 3. Energy dispersion of (a) H_1^{2D} in Eq. (6a) and (b) H_2^{2D} in Eq. (6b) for three different tilting parameters in the x direction t_x , and $t_y = 0$. The three tiltings correspond to the untilted type-I node, the node at the horizon, and the overtilted type-II node.

type-II case there is an electron (hole) pocket forming to the right (left) of the node.

The main difference between the two models, that will be relevant in later results, is that the red band in the overtilted region does not cross zero between $k = 0$ and $k = \pi$ in H_1^{1D} , but it does in H_2^{1D} . In the first model the electron and hole pockets extend throughout the whole Brillouin zone and they connect the two Weyl nodes, while in H_2^{1D} the pockets are finite and located next to the single node, which is the situation encountered in the band structure of type-II Weyl semimetals.

B. 2D and 3D lattice models

Similar to the 1D case, there are infinitely many ways to create 2D and 3D lattice models with a tilted Weyl cone around $k = 0$. Generalizing the two systems studied in 1D, we get the following Bloch Hamiltonians in 2D:

$$H_1^{2D} = (\sigma_x - t_x \sigma_0) \sin k_x + (\sigma_y - t_y \sigma_0) \sin k_y, \quad (6a)$$

$$H_2^{2D} = H_1^{2D} + \sigma_z (2 - \cos k_x - \cos k_y). \quad (6b)$$

Their dispersion relations are shown in Fig. 3. H_1^{2D} has four Weyl nodes in the entire Brillouin zone, while H_2^{2D} again only has a single Weyl node.

In 3D the Hamiltonian corresponding to H_2^{2D} does not exist, because the σ_z Pauli matrix was already used. This is consistent with the Nielsen-Ninomiya theorem [50], which does not allow a single Weyl node in a 3D lattice. The 3D equivalent of H_1^{1D} is

$$H_1^{3D} = \sum_i (\sigma_i - t_i \sigma_0) \sin k_i, \quad (7)$$

which has eight Weyl nodes. At $k_z = 0$ the dispersion relation is identical to that of H_1^{2D} , represented in Fig. 3(a).

C. Dirac equation in curved space-time

In the long-wavelength limit, the dynamics of the lattice models can be described by a low-energy continuum model. In particular, the effective Hamiltonians for the lattice Hamiltonians in Eqs. (4), (6), and (7) can be written (using Einstein

notation) as (see Appendix A for details)

$$H_{\text{eff}} = -i(\sigma_i - t_i \sigma_0) \partial_i - \frac{\sigma_0}{2i} \partial_i t_i, \quad (8)$$

where i runs on the spatial dimensions of the system ($d = 1, 2, 3$), and $t_i(x)$ are position-dependent tilting functions in different directions. The last term in Eq. (8) is required to make the Hamiltonian Hermitian. This equation can be thought of as a Dirac equation in a curved background. To explore this gravitational analogy in a more precise way, we introduce the metric [34,51–53]

$$ds^2 = (t^2 - 1)dT^2 - 2t_i dx_i dT + dx^2, \quad (9)$$

where T denotes the temporal coordinate, $t^2 = t_i t_i$, and $dx^2 = dx_i dx_i$. The massless Dirac equation for this background metric can be written in the form (see Appendix B)

$$\partial_T \Psi = \left(\gamma^{0i} \partial_i - t_i \partial_i - \frac{1}{2} \partial_i t_i - \frac{1}{4} (\partial_i t_j) \gamma^{ij} \right) \Psi, \quad (10)$$

where γ^0 and γ^i are the gamma matrices in flat space-time and by definition, $\gamma^{ab} = [\gamma^a, \gamma^b]/2$ for $a, b \in (0, 1, \dots, d)$. To link this equation to the Hamiltonian (8), we take the following representations for the gamma matrices:

$$\text{in (1+1)D: } \quad \gamma^0 = i\sigma_z, \quad \gamma^1 = \sigma_y, \quad (11)$$

$$\text{in (1+2)D: } \quad \gamma^0 = i\sigma_z, \quad \gamma^1 = \sigma_y, \quad \gamma^2 = -\sigma_x,$$

while in (1 + 3)D one may choose the Weyl representation

$$\gamma^0 = \begin{pmatrix} 0 & \sigma_0 \\ -\sigma_0 & 0 \end{pmatrix}, \quad \gamma^i = \begin{pmatrix} 0 & \sigma_i \\ \sigma_i & 0 \end{pmatrix}. \quad (12)$$

The Dirac equation on the gravitational background (9) coincides with the low-energy dynamical equation for the lattice models, provided the last term in Eq. (10) vanishes. In (1 + 1)D, this is always the case. In higher dimensions, we constrain the vector $t_i(x)$ to have a vanishing curl,

$$\partial_i t_j - \partial_j t_i = 0, \quad (13)$$

which cancels the last term in (10). Keeping this term would produce a spatially varying on-site potential in the tight-binding model. Since the term is proportional to the derivative of the tilting, its effect is negligible in systems with slowly varying tilting.

The region in space described by $t^2 - 1 = 0$ can be thought of as an event horizon. Notice that Eq. (9) represents a wide class of metrics, some of which are of particular importance in the context of gravitational physics (see, e.g., a recent discussion in [54]).

To simulate different metrics, we introduce spatial inhomogeneity in the tilting parameter. In the real-space Hamiltonians (3) we make the tilting parameter position dependent. This is different from previous models where the position dependence is in the Fermi velocity [45,47,55]. In this paper we will only consider effectively 1D horizons, so t_x will be a function of x and $t_{y/z} = 0$. In all cases the horizon will be defined by the points where $t_x = 1$.

III. WAVE-PACKET DYNAMICS

Now that we defined the systems of interest, we move on to study the propagation of wave packets in lattice models

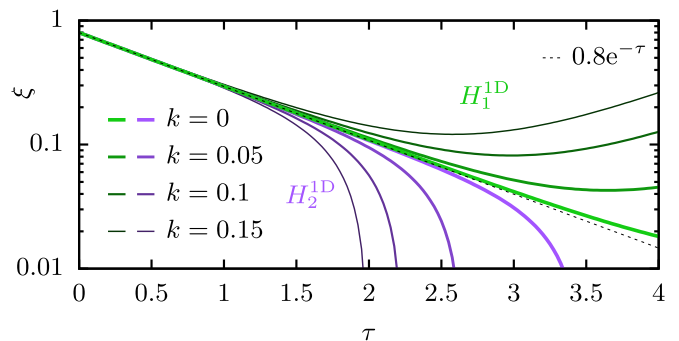


FIG. 4. Propagation of wave packets in a 1D lattice with a horizon. The figure shows the center of mass of the wave packet as a function of time for different starting momenta in systems H_1^{1D} and H_2^{1D} in Eq. (4). The rescaled position and time are defined as $\xi = 1 - 2x/L$ and $\tau = 2T/L$. The dashed line shows the geodesic calculated from Eq. (15). The length of the system is $L = 1000$.

with horizons. We study the different behaviors for our models with different horizons. We will show how the world lines of wave packets in our models match the geodesics of specific metrics, and we will simulate the propagation of Gaussian wave packets based on the Chebyshev expansion method. The details of this method are explained in Appendix C. The videos for all simulations discussed in the paper are included in Supplemental Material [56].

A. Linear horizon in 1D

First, we discuss 1D models with linearly changing tiltings $t_x = 2x/L$, where L is the length of the system. With this we linearly increase the tilting from $t = 0$ to $t = 2$ with the $t = 1$ horizon exactly at $L/2$. The systems we study are $L = 1000$ long. The starting wave packet is localized at $x_0 = 100$ in the red band of Fig. 2 and propagates to the right towards the horizon.

The red band becomes more and more flat approaching the horizon in both H_1^{1D} and H_2^{1D} . As a result, the group velocity of the wave packet gets smaller and smaller. While the wave packet is slowing down it becomes narrower. The time dependence of the position of the wave packet is shown in Fig. 4. For the figures we rescaled the position and time using $\xi = 1 - 2x/L$ and $\tau = 2T/L$. With this the wave packet moves from the initial position $\xi_0 = 0.8$ to the horizon $\xi = 0$.

The wave-packet dynamics results can be understood with a philosophy similar to that of the WKB approximation. Since the tilting parameter varies continuously and slowly with position, we can think of the system as being locally the infinite $H_{1/2}^{1D}(\mathbf{k})$. Since the tilting is proportional to σ_0 , the eigenvectors at different tiltings are all the same, from which it follows that states in the red or blue bands will stay eigenstates at whatever point of the chain. This means that a wave packet that is initially in the red (blue) band will stay in the red (blue) band. The system is not strictly homogeneous, and thus the momentum is not a conserved quantity; but since the inhomogeneity comes from a slow change in space, large jumps of the momentum are exponentially suppressed (this will be further clarified in Sec. IV). The quantity that is strictly conserved is the energy of the wave packet. By using the

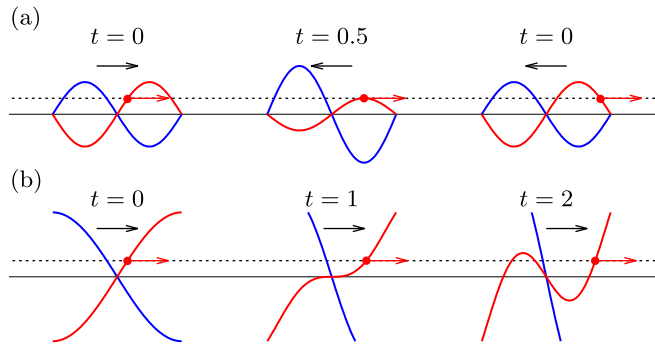


FIG. 5. Schematic representation for the propagation of wave packets with $E = 0.5$ in systems (a) H_1^{1D} and (b) H_2^{1D} . The local dispersion relation is shown at three points along the trajectory of the wave packets. The red dot represents the momentum of the wave packet, and the red arrow indicates the direction of change in this momentum. The black arrow shows the direction of the group velocity of the wave packet.

above-mentioned rules together with the dispersion relations in Fig. 2, the results of the 1D simulations can be explained.

First we discuss the H_1^{1D} system. Focusing on the red band, we see that it becomes completely flat at the horizon. If we take a packet with a small energy $E > 0$, the horizon is invisible for it since after a certain tilting there is no point in the red band that is at this energy. With a continuous slow change of the momentum, the state with energy E will go from $k = 0$ to $k = \pi$, and the group velocity will go from positive to negative while the wave packet bounces back from the horizon [see Fig. 5(a)]. The closer the energy is to 0, the closer the wave packet reaches the horizon, and in the limiting case of $E = 0$, the wave packet gets pinned to the horizon. On longer timescales, because of the lattice length scale that unavoidably comes into play [45], the wave packet slowly disintegrates and the center of mass will go towards the left. The behavior of the wave packets at different energies can be seen in Fig. 4 with the green curves.

The H_2^{1D} system is qualitatively very different from the H_1^{1D} system. Here, at every position there is an $E > 0$ state in the red band. This means that a finite-energy wave packet will go through the horizon with a continuous change in momentum [see Fig. 5(b)]. The zero-energy wave packet will slowly approach the horizon because of the zero group velocity at the horizon but eventually it will go through it. The behavior of the wave packets at different energies can be seen in Fig. 4 with the purple curves.

The time dependence of the wave packet approaching the horizon is consistent with the results in Ref. [45]. There, a one-band model with nearest-neighbor hopping was studied, where the hopping varies with the position. This can be understood, by coarse-graining, as a model with a linear dispersion close to zero energy, whose slope varies with position. The slope was set to zero at the origin of the lattice and finite away from it, thus mimicking the evolution of a light cone when moving away from a horizon. Since it has only one band, the hopping is exactly zero where the horizon is meant to be, meaning that the right and left side of the lattice are completely disconnected. In our two-band model this is not

the case, and as we saw in the H_2^{1D} system, the wave packet can propagate through the horizon.

It was shown in Refs. [45,46], both using numerical calculations and an analytical derivation based on a semiclassical approximation, that zero-energy wave packets propagating in the one-band model precisely follow the geodesics of a (1 + 1)D dilaton gravity. In the case where the hopping evolves linearly with position, these geodesics can be expressed as

$$1 - \alpha x(T) = e^{-\alpha(T-T_0)}, \quad (14)$$

where in our case $\alpha = 2/L$. Using the previously defined scaled position and time, this simply reads as

$$\xi(\tau) = \xi_0 e^{-\tau}. \quad (15)$$

As we can see in Fig. 4, this dependence is present for our models, too, with deviations only at larger timescales due to finite-size effects, when the size of the wave packet becomes comparable to the lattice constant.

B. Linear horizon in 2D and 3D

In 2D and 3D, wave packets propagate qualitatively differently from the 1D case. To understand the difference, we first consider a 2D system where $t_x = 0$ and $t_y = 0$ everywhere. A Gaussian wave packet centered at a large enough k will propagate based on the group velocity at k and will maintain its Gaussian shape. But getting closer to $k = 0$, this is no longer true. A wave packet with finite size in real space will also have a finite size in momentum space. This means that at low enough momenta the wave packet encapsulates the Weyl node and thus it will have components propagating in all directions radially. This behavior of the wave-packet propagation is shown in Fig. 6 with snapshots (in Supplemental Material the full animations are available).

In all simulations we choose the pseudospin components corresponding to the eigenvector of the infinite Hamiltonian with the average momentum of the wave packet. Because the eigenvectors are momentum dependent and because the wave packet includes multiple momenta, a zero-momentum wave packet includes a superposition of positive and negative energy states, which leads to *Zitterbewegung* of the electrons [57–60].

The world lines of the wave packets in 2D and 3D are shown in Figs. 7 and 8. Here we only focus on the center of mass of the wave packets on the x axis. As we can see, the results are very similar to the 1D results in Fig. 4. The main difference are the oscillations due to the *Zitterbewegung* at small times.

C. Power-law horizons in 1D

So far the tilting was always linearly dependent on the position; now we consider more generic cases and study how the different choices affect the wave-packet propagation. We only discuss the H_1^{1D} system, and for the H_2^{1D} model similar results can be obtained.

We consider models that follow a power law close to the horizon where $t = 1$. For the position dependence of the

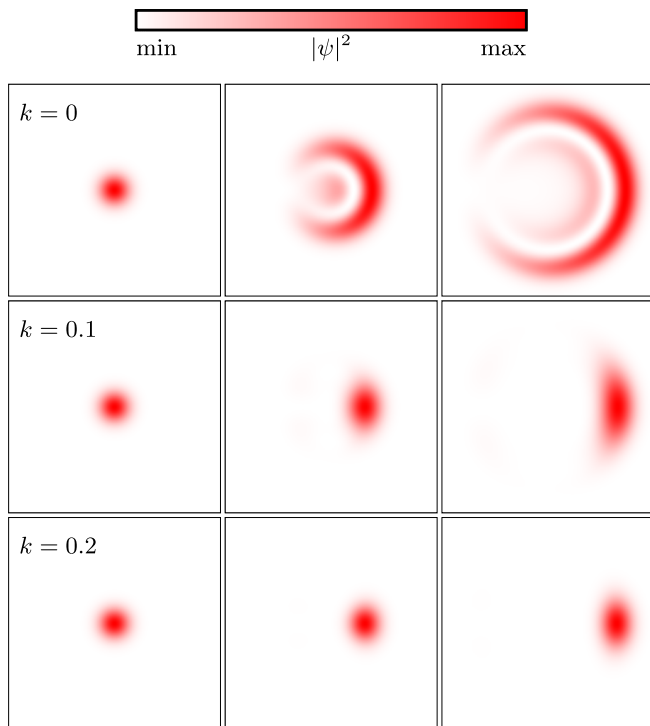


FIG. 6. Propagation of wave packets in the 2D systems without tilt. The figure shows snapshots of the wave packet for different starting momenta in the system H_1^{2D} . The length and width of the system are $L = 500$ and $W = 500$, and the initial wave packet has a width of 40 sites. The anisotropy in the top row is due to the specific pseudospin configuration of the initial wave packet.

tilting parameter we use

$$t(x) = 1 + \text{sgn}(2x - L) \left| \frac{2x}{L} - 1 \right|^\gamma, \quad (16)$$

where γ is the exponent. At $\gamma = 1$ we recover the model studied in the previous sections. This tilting dependence is shown in Fig. 9(a).

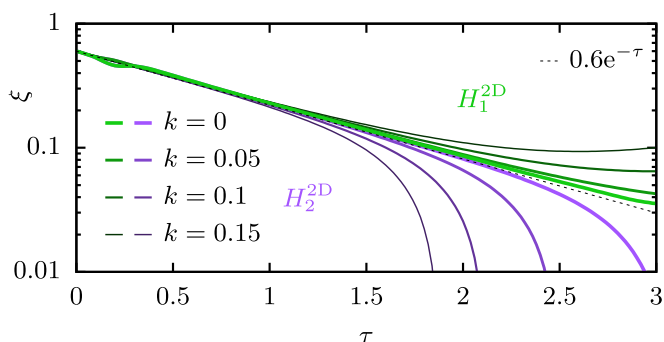


FIG. 7. Propagation of wave packets in a 2D lattice with a horizon. The figure shows the center of mass of the wave packet along the x axis as a function of time for different starting momenta in the systems H_1^{2D} and H_2^{2D} in Eq. (6). The rescaled position and time are defined as $\xi = 1 - 2x/L$ and $\tau = 2T/L$. The dashed line shows the geodesic calculated from Eq. (15). The length and width of the system are $L = 500$ and $W = 500$.

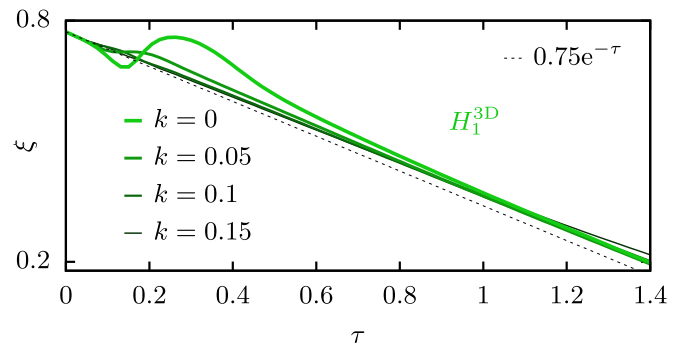


FIG. 8. Propagation of wave packets in a 3D lattice with a horizon. The figure shows the center of mass of the wave packet along the x axis as a function of time for different starting momenta in systems H_1^{3D} and H_2^{3D} in Eq. (6). The rescaled position and time are defined as $\xi = 1 - 2x/L$ and $\tau = 2T/L$. The dashed line shows the geodesic calculated from Eq. (15). The length, width, and height of the system are $L = 400$ (we only simulated the left half of the system), $W = 300$, and $H = 300$.

The world lines of the wave packet for different γ parameters are shown in Fig. 9(b). For linear and supralinear dependencies ($\gamma \geq 1$) we get wave packets that infinitely approach the horizon. The higher the exponent the slower

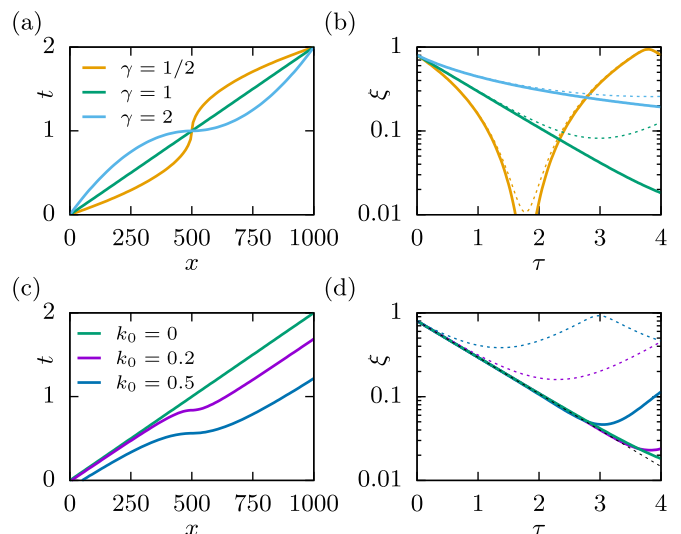


FIG. 9. Propagation of wave packets in a 1D lattice with different types of horizons using the H_1^{1D} system in Eq. (4). Panels (a, b) show the results for the tilting profile with different power laws as in Eq. (16) for three different γ exponents. Panels (c, d) show the results for the artificial horizons at finite momenta as in Eq. (20) for three different k_0 values. Panels (a) and (c) show the position dependence of the tilting parameter in the different horizon models. Panels (b) and (d) show the center of mass of the wave packet as a function of time for the models corresponding to panels (a) and (c). In panel (b) solid lines are with $k = 0$ and dashed lines with $k = 0.1$. In panel (d) solid lines are at tilting profiles and momenta corresponding to panel (c), while dashed lines are at momenta corresponding to panel (c) but with the linear tilting profile. The rescaled position and time are defined as $\xi = 1 - 2x/L$ and $\tau = 2T/L$. The length of the system in all panels is $L = 1000$.

the approach is. For sublinear dependencies ($\gamma < 1$) the wave packet goes very close to the horizon but ultimately bounces back from it. These results are consistent with the results obtained for the single-band model in Ref. [45].

D. Horizons for finite energy in 1D

In Secs. III A we saw that in the H_1^{1D} model, for the linear profile a wave packet at finite energies always deviates from the exponential time dependence and bounces back from the horizon. This happens because the effective horizon at finite energies is no longer at $t = 1$ but at lower values, and thus the wave packet cannot reach the center of the chain. Focusing on the red band in Fig. 2(a), the dispersion relation and group velocity are

$$E = (1 - t) \sin k, \tag{17a}$$

$$v = (1 - t) \cos k, \tag{17b}$$

which implies $v^2 = (1 - t)^2 - E^2$. Hence, for a wave packet of energy E , this means that there is an effective horizon at

$$1 - t(x_{\text{eff}}) = \pm E. \tag{18}$$

Knowing this, we can construct a tilting profile that has a horizon at finite energy similar to the zero-energy one. In order to reproduce the zero-energy world line we want a linearly decreasing group velocity:

$$v(x) = 1 - \frac{2x}{L}. \tag{19}$$

For $2x \leq L$ this can be satisfied by choosing

$$t(x) = 1 - \sqrt{\left(\frac{2x}{L} - 1\right)^2 + \left(\frac{2x_0}{L} - 1\right)^2 \tan^2 k_0}, \tag{20}$$

where k_0 is the initial momentum and x_0 is the initial position of the wave packet. For $2x > L$ we can choose an arbitrary tilting profile, since that part of the chain will not be accessible by the wave packet. For simplicity we use the same dependency but flipped. The tilting parameter as a function of position is shown in Fig. 9(c). Using these horizons, the wave-packet world lines are shown in Fig. 9(d). As we can see, the world lines that were bouncing back with the linear profile at finite momenta now are approaching the horizon similarly to the $k = 0$ wave packet. Close to the horizon because of lattice effects we get the disintegration of the wave packet similarly to the $k = 0$ case.

IV. SCATTERING MATRIX

To characterize the different possible scenarios in the models discussed above, we turn to scattering theory. Taking the same systems studied in Sec. III A, we attach two semi-infinite leads on both ends. We restrict the discussion to 1D systems, because with the change in tilting always being in one direction only, we can always choose periodic boundary conditions in the other directions to get effectively 1D systems. The leads are made using the same model as the system with fixed tilting $t = 0$ ($t = 2$) for the left (right) lead. For the scattering region we take a 1000-sites-long chain. We then calculate

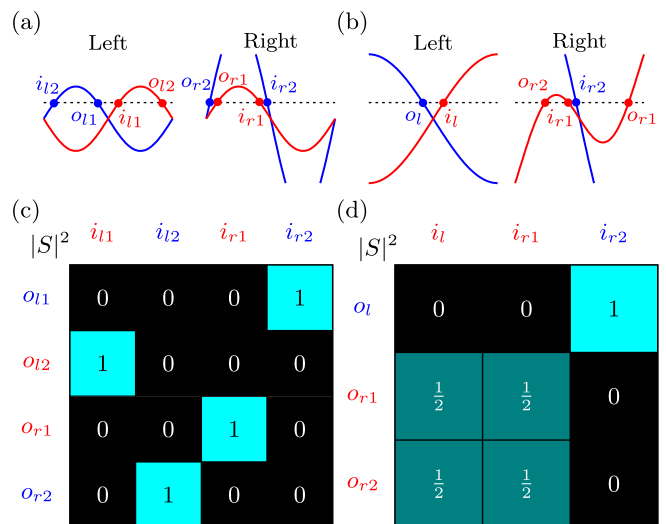


FIG. 10. Propagating modes and scattering matrix of the H_1^{1D} (a, c) and H_2^{1D} (b, d) lattice models with a horizon. In panels (a) and (b) the dispersion relations in the left and right leads are shown. At the energy indicated by the dashed line, the possible propagating modes are indicated by the filled circles. In panels (c) and (d), the scattering probabilities between the modes at zero energy are shown. The length of the scattering region is $L = 1000$.

the scattering matrix between the two leads numerically using the KWANT package [61]. The scattering matrix (S) encodes the probability amplitudes of scattering from incoming modes (\mathbf{i}) into outgoing modes (\mathbf{o}):

$$o_m = \sum_n S_{mn}(\varepsilon) i_n, \tag{21}$$

where ε is the energy of the considered modes.

First, we discuss the H_1^{1D} system. The propagating modes at a given $\varepsilon > 0$ energy in this system are shown in Fig. 10(a). There are two incoming and two outgoing modes in each side of the scattering region, resulting in a scattering matrix that is 4×4 . The scattering matrix at $\varepsilon = 0$ is shown in Fig. 10(c). We can see that each incoming mode is scattered into an outgoing mode with probability 1. Incoming modes from the red bands are totally reflected into outgoing modes in the red band of the same lead. Incoming modes of the blue bands are completely transmitted into outgoing modes in the blue band of the opposite lead. This behavior is consistent with the reasoning of the previous section: the red band becomes completely flat so states in this band cannot cross the horizon, while the blue band stays qualitatively the same and the states in this band can go through the horizon. The same is valid for all energies, as long as there are propagating modes in both leads.

Then we study the H_2^{1D} system. The propagating modes at a given $\varepsilon > 0$ energy in this system are shown in Fig. 10(b). The left lead has one incoming and one outgoing mode while the right lead has two and two, resulting in a scattering matrix that is 3×3 . The scattering matrix at $\varepsilon = 0$ is shown in Fig. 10(d). The incoming mode in the blue band is totally transmitted into the outgoing mode in the blue band. At zero energy the incoming modes in the red band are equally split between

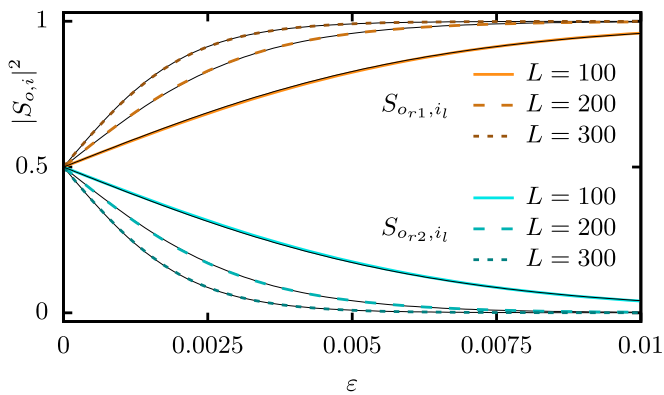


FIG. 11. Energy dependence of the scattering probability from the incoming mode i_l to the outgoing modes o_{r1} and o_{r2} from Fig. 10(b). The colored lines show the numerical results for different system lengths. The solid black lines show the analytic formulas in Eq. (22).

the two outgoing modes in the red band. In this system there is a big difference between the red incoming mode on the left and right sides. Starting from the left side we get total transmission, while starting from the right side we get total reflection.

In the H_2^{1D} system the energy dependence of the scattering amplitudes is more complicated than the H_1^{1D} system. The zeros and ones are unaffected, but the equal splitting between the red bands is only valid at $\varepsilon = 0$. Let us consider the i_l incoming mode. At a large enough positive energy, if we follow the same energy modes throughout the scattering region we see that they appear at continuously increasing momenta until we reach a large enough tilting at the other side of the horizon, where a second same energy mode appears at a very different negative momentum. Since large momentum changes are not allowed because of the slow varying of the tilting, the i_l mode will be totally transmitted into the o_{r1} mode at large enough positive energies. The closer we go to zero energy we see that at the point of the appearance of the second mode with the same energy, the difference between the two momenta is decreased, and at $\varepsilon = 0$ it is equal to zero. This means that the i_l mode can scatter into both the o_{r1} and o_{r2} with continuous momentum change, and thus they have equal scattering probabilities. In between the zero and the high enough energies, the scattering probabilities show an exponential behavior (see Fig. 11)

The same was observed for the H_2^{1D} Hamiltonian for a similar tilting dependency in Refs. [27,28]. The energy dependence of the scattering rate can be expressed as

$$|S_{o_{r1}, i_l}|^2 = \frac{1}{1 + e^{\pi L \varepsilon}}, \quad (22a)$$

$$|S_{o_{r2}, i_l}|^2 = 1 - \frac{1}{1 + e^{\pi L \varepsilon}}. \quad (22b)$$

We see that the momentum jumps are exponentially suppressed. Increasing the system size makes the change of tilting smoother, which in turn makes the quasiconservation of momentum stricter and causes the probability amplitudes to reach their asymptotic behavior faster. The *Hawking fragmentation* coined in Ref. [27] can thus be understood as intermode

scattering between multiple states at the same energy with different momenta. Increasing the energy of the incoming mode increases the momentum difference between the scattered modes, which leads to the energy dependence shown in Fig. 11.

V. DISCUSSION AND CONCLUSIONS

We introduced lattice models for tilted WSMs where the tilting varies smoothly with position. These models at small momenta effectively correspond to the massless Dirac equation in a curved space-time background. To understand the role of high momenta and inter-Weyl-node effects, we studied two different types of systems: the first type (H_1) has 2^d nodes where d is the dimension of the system, while the second type (H_2) only has a single Weyl node.

Using these models, we simulated wave-packet propagations for three types of tilting profiles in 1D, 2D, and 3D using the Chebyshev expansion method. When the tilting varies linearly with position, and in the zero-energy limit of both H_1 and H_2 , the wave packets follow the geodesics of $(1+1)D$ de Sitter space-time, as found previously in a single-band model [45]. At finite energies ($E > 0$) though, H_1 and H_2 give very different behaviors. H_1 causes wave packets to bounce back, similarly to the single-band model, while H_2 causes wave packets to be transmitted. This is explained by the differences in the band structure at large momenta, which allow for scattering to same-energy states in H_2 but not in H_1 . When the tilting varies as a power law with position, we found that the transition between models with and without a horizon found in the single-band model is also present in two-band models. Finally, we designed a specific tilting profile that moves the horizon away from zero energy and can be tuned to obtain eternal slowing down for any initial wave packet.

We showed that these results can be understood using the local dispersion relations, the conservation of energy, and only allowing continuous change for the quasimomentum. To further show the validity of this approach, we computed the scattering matrix for 1D systems, which corresponds well to this analysis. In H_2 , due to the presence of multiple states at a single energy, intermode scattering occurs, in agreement with scattering amplitudes obtained in a related model [27,28], which we now relate directly to wave-packet trajectories. In the H_1 system, though, we only found fully transmitted or reflected modes without any scattering taking place.

The models studied in this paper are simplified versions of more realistic systems where one might observe horizon physics experimentally. In real materials such as the previously mentioned $Zn_2In_2S_5$ [38], disorder and interactions should be taken into account to have a complete description. Such calculations are still an open problem, and the effects they might have on the phenomena discussed in this paper require further studies. On the other hand, effective systems that have horizons can be created using metamaterials such as in Refs. [62–67]. The advantage of these systems is the better control over the tilting parameter, which can be engineered by inhomogeneously creating the metamaterial.

In summary, our results bridge the gap between the single-band description and concrete proposals for the experimental realization of Weyl gravitational analogs. Indeed, they point

to the rich physics arising from the presence of a second band and the presence or absence of other Weyl nodes at large momenta. These can in some cases dominate the observed phenomena and therefore indicate limitations of the analogy between tilted WSMs and gravitational systems, which should be taken into account in experimental setups. Finally, we identified the possibility of tuning the tilting profile to provide horizons for finite-energy wave packets, thus expanding the possibilities offered by this type of gravitational analog.

ACKNOWLEDGMENTS

The authors are grateful to I. C. Fulga for helpful discussions on the subject. We thank Ulrike Nitzsche for technical assistance. A.G.M. acknowledges support by the Academy of Finland Project No. 331094.

APPENDIX A: CONNECTION BETWEEN TIGHT-BINDING AND CONTINUUM MODELS

In this section we show how the tight-binding Hamiltonians in Eq. (3) become the Eq. (8) continuum model when going to vanishing lattice constants. We only show H_1^{1D} in detail; H_2^{1D} and higher dimensions can be derived similarly. The single-particle tight-binding eigenvalue problem can be written as

$$E\psi_n = (\sigma_x - t_n\sigma_0)\frac{\psi_{n+1}}{2i} - (\sigma_x - t_{n-1}\sigma_0)\frac{\psi_{n-1}}{2i}. \quad (\text{A1})$$

We can regroup terms in the same equation as

$$\frac{E}{a}\psi_n = (\sigma_x - t_n\sigma_0)\frac{\psi_{n+1} - \psi_{n-1}}{2ia} - \frac{t_n - t_{n-1}}{2ia}\psi_{n-1}, \quad (\text{A2})$$

where we divided the equation with the lattice constant a . Approximating derivatives with finite differences as

$$\partial_x\psi \leftrightarrow \frac{\psi_{n+1} - \psi_{n-1}}{2a}, \quad (\text{A3})$$

$$\partial_x t \leftrightarrow \frac{t_n - t_{n-1}}{a}, \quad (\text{A4})$$

and rescaling the energy with the lattice constant we get the Hamiltonian in Eq. (8),

$$E\psi(x) = -i(\sigma_i - t_i\sigma_0)\partial_x\psi(x) - \frac{\sigma_0}{2i}[\partial_x t(x)]\psi(x). \quad (\text{A5})$$

APPENDIX B: DERIVATION OF THE DIRAC EQUATION

Here we will derive Eq. (10) explicitly. In what follows, we use the conventions for representation of the Dirac equation and the exterior algebra technique, which can be found, e.g., in Ref. [68]. The general expression of the massless Dirac equation in a curved background is given by

$$\gamma^a e_a^\mu (\partial_\mu + \frac{1}{4}\omega_\mu^{ab}\gamma_{ab})\Psi = 0, \quad (\text{B1})$$

where e_a^μ is the inversed frame field and ω_μ^{ab} is the spin connection. Any metric can be written in terms of frame fields, e^a_μ , as $g_{\mu\nu} = \eta_{ab}e^a_\mu e^b_\nu$, where η_{ab} is the Minkowski metric $\eta_{ab} = \text{diag}(-, +, \dots, +)$. Given the metric (9), the corresponding frame field one-forms are

$$e^0_\mu dx^\mu = dT, \quad e^i_\mu dx^\mu = dx^i - t^i dT, \quad (\text{B2})$$

while the inversed frame fields e_a^μ , contributing to Eq. (B1), read

$$e_0^\mu \partial_\mu = \partial_T + t_i \partial_i, \quad e_i^\mu \partial_\mu = \partial_i. \quad (\text{B3})$$

Thus the first term in Eq. (B1) is

$$\gamma^a e_a^\mu \partial_\mu = \gamma^0 (\partial_T + t_i \partial_i) + \gamma^i \partial_i. \quad (\text{B4})$$

In order to find the second term in Eq. (B1), we need to calculate the spin connection ω_μ^{ab} . The spin connection one-form ω^{ab} has to satisfy the torsion-free condition

$$de^a + \omega^a_b \wedge e^b = 0, \quad (\text{B5})$$

where \wedge stands for the wedge product, while d denotes the exterior derivative. Taking into account the explicit form of e^a given in Eq. (B2) for our metric, the equations above can be written as

$$\omega^{0i} \wedge e^i = 0, \quad (\text{B6})$$

$$\partial_j t^i dx^j \wedge dT - \omega^{0i} \wedge dT - \omega^{ij} \wedge e^j = 0.$$

Note that i, j are raised and lowered by the Euclidean metric and, as before, the summation is assumed over repeating indices. Considering these relations as a set of algebraic linear equations for components of the spin connection ω^{ab} , one finds

$$\omega_\mu^{0i} dx^\mu = \frac{1}{2}(\partial^i t_j + \partial_j t^i)e^j, \quad (\text{B7})$$

$$\omega_\mu^{ij} dx^\mu = \frac{1}{2}(\partial^i t^j - \partial^j t^i)dT,$$

where e^j are given in Eq. (B2). Now we are ready to find the second term of Eq. (B1) in the explicit form

$$\frac{1}{4}\gamma^a e_a^\mu \omega_\mu^{ab} \gamma_{ab} = \frac{1}{2}\gamma^0 \partial_i t_i + \frac{1}{4}\gamma^{ij} \gamma^0 \partial_i t_j. \quad (\text{B8})$$

Putting Eqs. (B4) and (B8) together and multiplying the resulting expression by γ^0 , one finds Eq. (10).

APPENDIX C: CHEBYSHEV EXPANSION METHOD

The time evolution of wave packets was performed using the Chebyshev expansion method [48,49]. The method is based on the following expansion of the exponential function:

$$e^{-itx} = J_0(t) + 2 \sum_{m=1}^{\infty} (-i)^m J_m(t) T_m(x), \quad (\text{C1})$$

where J_m are the Bessel functions of the first kind, and T_m are the Chebyshev polynomials of the first kind. This formula is valid in the range $x \in [-1, 1]$. The Chebyshev polynomials can be obtained using the following recurrence relation:

$$T_{m+1}(x) + T_{m-1}(x) = 2xT_m(x), \quad (\text{C2a})$$

$$T_0(x) = 1, \quad (\text{C2b})$$

$$T_1(x) = x. \quad (\text{C2c})$$

This expansion can be used to calculate the time evolution of $|\psi(0)\rangle$:

$$|\psi(t)\rangle = e^{-iHt} |\psi(0)\rangle. \quad (\text{C3})$$

Using Eq. (C1) we get

$$|\psi(t)\rangle = J_0(t) |\psi(0)\rangle + 2 \sum_{m=1}^{\infty} (-i)^m J_m(t) T_m(H) |\psi(0)\rangle. \quad (\text{C4})$$

In order for the Chebyshev expansion to be convergent, the Hamiltonian has to be normalized such that each eigen-

value is in the range $[-1, 1]$. Using the recurrence relation in Eq. (C2),

$$T_0(H) |\psi\rangle = |\psi\rangle, \quad (\text{C5a})$$

$$T_1(H) |\psi\rangle = H |\psi\rangle, \quad (\text{C5b})$$

$$T_{m+1}(H) |\psi\rangle = [2HT_m(H) - T_{m-1}(H)] |\psi\rangle. \quad (\text{C5c})$$

This algorithm does not require the eigenvalue problem of the Hamiltonian to be solved. By using sparse matrices, the recurrence relation can be evaluated efficiently, allowing us to study much larger systems than those accessible with methods that require the diagonalization of the Hamiltonian.

-
- [1] W. G. Unruh, Experimental Black-Hole Evaporation?, *Phys. Rev. Lett.* **46**, 1351 (1981).
- [2] L. C. B. Crispino, A. Higuchi, and G. E. A. Matsas, The Unruh effect and its applications, *Rev. Mod. Phys.* **80**, 787 (2008).
- [3] S. W. Hawking, Black hole explosions?, *Nature (London)* **248**, 30 (1974).
- [4] S. W. Hawking, Particle creation by black holes, *Commun. Math. Phys.* **43**, 199 (1975).
- [5] D. N. Page, Hawking radiation and black hole thermodynamics, *New J. Phys.* **7**, 203 (2005).
- [6] C. Barceló, S. Liberati, and M. Visser, Analogue gravity from Bose-Einstein condensates, *Classical Quantum Gravity* **18**, 1137 (2001).
- [7] T. G. Philbin, C. Kuklewicz, S. Robertson, S. Hill, F. König, and U. Leonhardt, Fiber-optical analog of the event horizon, *Science* **319**, 1367 (2008).
- [8] I. Carusotto, S. Fagnocchi, A. Recati, R. Balbinot, and A. Fabbri, Numerical observation of Hawking radiation from acoustic black holes in atomic Bose-Einstein condensates, *New J. Phys.* **10**, 103001 (2008).
- [9] C. Barceló, S. Liberati, and M. Visser, Analogue gravity, *Living Rev. Relativity* **14**, 3 (2011).
- [10] O. Boada, A. Celi, J. I. Latorre, and M. Lewenstein, Dirac equation for cold atoms in artificial curved spacetimes, *New J. Phys.* **13**, 035002 (2011).
- [11] F. Caravelli, A. Hamma, F. Markopoulou, and A. Riera, Trapped surfaces and emergent curved space in the Bose-Hubbard model, *Phys. Rev. D* **85**, 044046 (2012).
- [12] L. Sindoni, Emergent models for gravity: An overview of microscopic models, *SIGMA. Symmetry, Integr. Geom. Methods Appl.* **8**, 027 (2012).
- [13] H. S. Nguyen, D. Gerace, I. Carusotto, D. Sanvitto, E. Galopin, A. Lemaître, I. Sagnes, J. Bloch, and A. Amo, Acoustic Black Hole in a Stationary Hydrodynamic Flow of Microcavity Polaritons, *Phys. Rev. Lett.* **114**, 036402 (2015).
- [14] J. Minář and B. Grémaud, Mimicking Dirac fields in curved spacetime with fermions in lattices with non-unitary tunneling amplitudes, *J. Phys. A: Math. Theor.* **48**, 165001 (2015).
- [15] A. Celi, Different models of gravitating Dirac fermions in optical lattices, *Eur. Phys. J.: Spec. Top.* **226**, 2729 (2017).
- [16] J. Dubail, J.-M. Stéphane, and P. Calabrese, Emergence of curved light-cones in a class of inhomogeneous Luttinger liquids, *Sci. Post Phys.* **3**, 019 (2017).
- [17] A. Roldán-Molina, A. S. Nunez, and R. A. Duine, Magnonic Black Holes, *Phys. Rev. Lett.* **118**, 061301 (2017).
- [18] J. Rodríguez-Laguna, L. Tarruell, M. Lewenstein, and A. Celi, Synthetic Unruh effect in cold atoms, *Phys. Rev. A* **95**, 013627 (2017).
- [19] A. Kosior, M. Lewenstein, and A. Celi, Unruh effect for interacting particles with ultracold atoms, *Sci. Post Phys.* **5**, 061 (2018).
- [20] A. J. Kollár, M. Fitzpatrick, and A. A. Houck, Hyperbolic lattices in circuit quantum electrodynamics, *Nature (London)* **571**, 45 (2019).
- [21] J. Nissinen, Emergent Spacetime and Gravitational Nieh-Yan Anomaly in Chiral $p + ip$ Weyl Superfluids and Superconductors, *Phys. Rev. Lett.* **124**, 117002 (2020).
- [22] I. Boettcher, P. Bienias, R. Belyansky, A. J. Kollár, and A. V. Gorshkov, Quantum simulation of hyperbolic space with circuit quantum electrodynamics: From graphs to geometry, *Phys. Rev. A* **102**, 032208 (2020).
- [23] B. Lapiere, K. Choo, C. Tauber, A. Tiwari, T. Neupert, and R. Chitra, Emergent black hole dynamics in critical Floquet systems, *Phys. Rev. Res.* **2**, 023085 (2020).
- [24] T. Farajollahpour, Z. Faraei, and S. A. Jafari, Solid-state platform for space-time engineering: The $8pmmn$ borophene sheet, *Phys. Rev. B* **99**, 235150 (2019).
- [25] I. Boettcher, A. V. Gorshkov, A. J. Kollár, J. Maciejko, S. Rayan, and R. Thomale, Crystallography of hyperbolic lattices, *Phys. Rev. B* **105**, 125118 (2022).
- [26] B. Mula, S. N. Santalla, and J. Rodríguez-Laguna, Casimir forces on deformed fermionic chains, *Phys. Rev. Res.* **3**, 013062 (2021).
- [27] D. Sabsovich, P. Wunderlich, V. Fleurov, D. I. Pikulin, R. Ilan, and T. Meng, Hawking fragmentation and Hawking attenuation in Weyl semimetals, *Phys. Rev. Res.* **4**, 013055 (2022).
- [28] C. De Beule, S. Groenendijk, T. Meng, and T. L. Schmidt, Artificial event horizons in Weyl semimetal heterostructures and their non-equilibrium signatures, *Sci. Post Phys.* **11**, 095 (2021).
- [29] M. Stålhammar, J. Larana-Aragon, L. Rødland, and F. K. Kunst, \mathcal{PT} symmetry-protected exceptional cones and analogue Hawking radiation, [arXiv:2106.05030](https://arxiv.org/abs/2106.05030).
- [30] S. Weinfurter, E. W. Tedford, M. C. J. Penrice, W. G. Unruh, and G. A. Lawrence, Measurement of Stimulated Hawking Emission in an Analogue System, *Phys. Rev. Lett.* **106**, 021302 (2011).

- [31] J. Steinhauer, Observation of quantum Hawking radiation and its entanglement in an analogue black hole, *Nat. Phys.* **12**, 959 (2016).
- [32] J. Hu, L. Feng, Z. Zhang, and C. Chin, Quantum simulation of Unruh radiation, *Nat. Phys.* **15**, 785 (2019).
- [33] N. P. Armitage, E. J. Mele, and A. Vishwanath, Weyl and Dirac semimetals in three-dimensional solids, *Rev. Mod. Phys.* **90**, 015001 (2018).
- [34] G. E. Volovik, Black hole and Hawking radiation by Type-II Weyl fermions, *JETP Lett.* **104**, 645 (2016).
- [35] G. E. Volovik, *The Universe in a Helium Droplet* (Oxford University Press, Oxford, 2003), Vol. 117.
- [36] A. Westström and T. Ojanen, Designer Curved-Space Geometry for Relativistic Fermions in Weyl Metamaterials, *Phys. Rev. X* **7**, 041026 (2017).
- [37] S. Guan, Z.-M. Yu, Y. Liu, G.-B. Liu, L. Dong, Y. Lu, Y. Yao, and S. A. Yang, Artificial gravity field, astrophysical analogues, and topological phase transitions in strained topological semimetals, *npj Quantum Mater.* **2**, 23 (2017).
- [38] H. Huang, K.-H. Jin, and F. Liu, Black-hole horizon in the Dirac semimetal $\text{Zn}_2\text{In}_2\text{S}_5$, *Phys. Rev. B* **98**, 121110(R) (2018).
- [39] L. Liang and T. Ojanen, Curved spacetime theory of inhomogeneous Weyl materials, *Phys. Rev. Res.* **1**, 032006(R) (2019).
- [40] V. Arjona and M. A. H. Vozmediano, Rotational strain in Weyl semimetals: A continuum approach, *Phys. Rev. B* **97**, 201404(R) (2018).
- [41] M. P. Ghimire, J. I. Facio, J.-S. You, L. Ye, J. G. Checkelsky, S. Fang, E. Kaxiras, M. Richter, and J. van den Brink, Creating Weyl nodes and controlling their energy by magnetization rotation, *Phys. Rev. Res.* **1**, 032044(R) (2019).
- [42] Y. Ferreiros, Y. Kedem, E. J. Bergholtz, and J. H. Bardarson, Mixed Axial-Torsional Anomaly in Weyl Semimetals, *Phys. Rev. Lett.* **122**, 056601 (2019).
- [43] L. Liang and T. Ojanen, Topological magnetotorsional effect in Weyl semimetals, *Phys. Rev. Res.* **2**, 022016(R) (2020).
- [44] C.-K. Chan, Y.-T. Oh, J. H. Han, and P. A. Lee, Type-II Weyl cone transitions in driven semimetals, *Phys. Rev. B* **94**, 121106(R) (2016).
- [45] C. Morice, A. G. Moghaddam, D. Chernyavsky, J. van Wezel, and J. van den Brink, Synthetic gravitational horizons in low-dimensional quantum matter, *Phys. Rev. Res.* **3**, L022022 (2021).
- [46] C. Morice, D. Chernyavsky, J. van Wezel, J. van den Brink, and A. G. Moghaddam, Quantum dynamics in 1D lattice models with synthetic horizons, [arXiv:2112.12827](https://arxiv.org/abs/2112.12827).
- [47] A. G. Moghaddam, D. Chernyavsky, C. Morice, J. van Wezel, and J. van den Brink, Engineering spectral properties of non-interacting lattice Hamiltonians, *Sci. Post Phys.* **11**, 109 (2021).
- [48] R. Kosloff, Propagation methods for quantum molecular dynamics, *Annu. Rev. Phys. Chem.* **45**, 145 (1994).
- [49] A. Weiße, G. Wellein, A. Alvermann, and H. Fehske, The kernel polynomial method, *Rev. Mod. Phys.* **78**, 275 (2006).
- [50] H. B. Nielsen and M. Ninomiya, Absence of neutrinos on a lattice. I. Proof by homotopy theory, *Nucl. Phys. B* **185**, 20 (1981).
- [51] J. Nissinen and G. E. Volovik, Type-III and IV interacting Weyl points, *JETP Lett.* **105**, 447 (2017).
- [52] T. Farajollahpour and S. A. Jafari, Synthetic non-Abelian gauge fields and gravitomagnetic effects in tilted Dirac cone systems, *Phys. Rev. Res.* **2**, 023410 (2020).
- [53] Y. Kedem, E. J. Bergholtz, and F. Wilczek, Black and white holes at material junctions, *Phys. Rev. Res.* **2**, 043285 (2020).
- [54] G. E. Volovik, Macroscopic quantum tunneling: From quantum vortices to black holes and universe, [arXiv:2108.00419](https://arxiv.org/abs/2108.00419).
- [55] N. M. R. Peres, Scattering in one-dimensional heterostructures described by the Dirac equation, *J. Phys.: Condens. Matter* **21**, 095501 (2009).
- [56] See Supplemental Material at <http://link.aps.org/supplemental/10.1103/PhysRevResearch.4.033237> for videos containing the wave-packet simulation results.
- [57] E. Schrödinger, Über die kräftefreie Bewegung in der relativistischen quantenmechanik, *Sitzungsber. Peuss. Akad. Wiss., Phys. Math. Kl.* **24**, 418 (1930).
- [58] A. O. Barut and A. J. Bracken, Zitterbewegung and the internal geometry of the electron, *Phys. Rev. D* **23**, 2454 (1981).
- [59] V. Y. Demikhovskii, G. M. Maksimova, A. A. Perov, and E. V. Frolova, Space-time evolution of Dirac wave packets, *Phys. Rev. A* **82**, 052115 (2010).
- [60] V. Y. Demikhovskii, G. M. Maksimova, and E. V. Frolova, Wave packet dynamics in a two-dimensional electron gas with spin orbit coupling: Splitting and zitterbewegung, *Phys. Rev. B* **78**, 115401 (2008).
- [61] C. W. Groth, M. Wimmer, A. R. Akhmerov, and X. Waintal, Kwant: A software package for quantum transport, *New J. Phys.* **16**, 063065 (2014).
- [62] Z. Yang and B. Zhang, Acoustic Type-II Weyl Nodes from Stacking Dimerized Chains, *Phys. Rev. Lett.* **117**, 224301 (2016).
- [63] B. Xie, H. Liu, H. Cheng, Z. Liu, S. Chen, and J. Tian, Experimental Realization of Type-II Weyl Points and Fermi Arcs in Phononic Crystal, *Phys. Rev. Lett.* **122**, 104302 (2019).
- [64] T. Ozawa, H. M. Price, A. Amo, N. Goldman, M. Hafezi, L. Lu, M. C. Rechtsman, D. Schuster, J. Simon, O. Zilberberg, and I. Carusotto, Topological photonics, *Rev. Mod. Phys.* **91**, 015006 (2019).
- [65] M. Miličević, G. Montambaux, T. Ozawa, O. Jamadi, B. Real, I. Sagnes, A. Lemaître, L. Le Gratiet, A. Harouri, J. Bloch, and A. Amo, Type-III and Tilted Dirac Cones Emerging from Flat Bands in Photonic Orbital Graphene, *Phys. Rev. X* **9**, 031010 (2019).
- [66] F. Zangeneh-Nejad and R. Fleury, Zero-Index Weyl Metamaterials, *Phys. Rev. Lett.* **125**, 054301 (2020).
- [67] S. M. Rafi-Ul-Islam, Z. Bin Siu, and M. B. Jalil, Topoelectrical circuit realization of a Weyl semimetal heterojunction, *Commun. Phys.* **3**, 72 (2020).
- [68] D. Z. Freedman and A. Van Proeyen, *Supergravity* (Cambridge University Press, Cambridge, England, 2012).